Mon. Not. R. Astron. Soc. **351,** 607–616 (2004) doi:10.1111/j.1365-2966.2004.07807.x

The structure of brown dwarf circumstellar discs

Christina Walker,[1★] Kenneth Wood,[1] C. J. Lada,[2] Thomas Robitaille,[1] J. E. Bjorkman[3] and Barbara Whitney[4]

[1]*School of Physics & Astronomy, University of St Andrews, North Haugh, St Andrews KY16 9SS*
[2]*Harvard-Smithsonian Center for Astrophysics, 60 Garden Street, Cambridge, MA 02138, USA*
[3]*Ritter Observatory, Department of Physics & Astronomy, University of Toledo, Toledo, OH 43606, USA*
[4]*Space Science Institute, 3100 Marine Street, Suite A353, Boulder, CO 80303, USA*

Accepted 2004 March 3. Received 2004 February 16; in original form 2003 September 17

ABSTRACT

We present synthetic spectra for circumstellar discs that are heated by radiation from a central brown dwarf. Under the assumption of vertical hydrostatic equilibrium, our models yield scaleheights for brown dwarf discs in excess of three times those derived for classical T Tauri (CTTS) discs. If the near-IR excess emission observed from brown dwarfs is indeed due to circumstellar discs, then the large scaleheights we find could have a significant impact on the optical and near-IR detectability of such systems. Our radiation transfer calculations show that such highly flared discs around brown dwarfs will result in a large fraction of obscured sources due to extinction of direct starlight by the disc over a wide range of sightlines. The obscured fraction for a 'typical' CTTS is less than 20 per cent. We show that the obscured fraction for brown dwarfs may be double that for CTTS, but this depends on stellar and disc mass. We also comment on possible confusion in identifying brown dwarfs via colour–magnitude diagrams: edge-on CTTS display similar colours and magnitudes to face-on brown dwarf plus disc systems.

Key words: circumstellar matter – stars: low-mass, brown dwarfs – stars: pre-main-sequence – infrared: stars.

1 INTRODUCTION

Observational evidence, including near-IR (Oasa, Tamura & Sugitani 1999; Muench et al. 2001; Liu, Najita & Tokunaga 2003) and mid-IR excess emission (Comerón et al. 1998; Comerón, Neuhauser & Kaas 2000), and Hα signatures of accretion (Muzerolle et al. 2000), indicates the presence of circumstellar discs around brown dwarfs. The existence of circumstellar discs around brown dwarfs is an important discovery, since it may suggest that brown dwarfs form in a similar fashion to more massive T Tauri stars (Shu, Adams & Lizano 1987). At the same time, data indicating significant masses and extents of circumstellar material may cause problems for brown dwarf formation scenarios in which the low-mass object is formed and subsequently ejected from a multiple system (Reipurth & Clarke 2001).

The observed spectral energy distributions (SEDs) and IR excess emission of some brown dwarfs have been modelled using flat and flared reprocessing discs (e.g. Natta & Testi 2001; Testi et al. 2002; Liu et al. 2003). The SED models suggest that brown dwarf discs are similar to those around CTTS. Models for the SEDs and scattered-light images of CTTS require flared discs (e.g. Kenyon & Hartmann 1987; D'Alessio et al. 1999; Whitney & Hartmann 1992; Burrows et al. 1996). For highly inclined flared discs, direct starlight is blocked by the optically thick disc, resulting in a fraction of sources that will appear very faint in the optical and near-IR. Such faint or 'optically obscured' sources may escape detection in magnitude-limited surveys. The degree of disc flaring depends on the disc temperature structure and the mass of the central star, with the disc scaleheight $h \propto (T_{\rm d}/M_\star)^{1/2}$ (Shakura & Sunyaev 1973). Therefore, low-mass brown dwarfs may have discs that are more vertically extended than those around CTTS and, depending on the disc mass, the obscured fraction may be larger. We will show that this may lead to confusion in discriminating between brown dwarfs and edge-on CTTS.

In this paper we adopt the same working hypothesis as Natta & Testi (2001), namely that brown dwarf discs are in vertical hydrostatic equilibrium with dust and gas well mixed throughout the disc. Such disc models have been very successful in explaining the observed scattered-light images and SEDs of CTTS. We extend our Monte Carlo radiative equilibrium code to calculate the structure of passively heated brown dwarf discs in vertical hydrostatic

★E-mail: cw26@st-andrews.ac.uk (CW); kw25@st-andrews.ac.uk (KW); clada@cfa.harvard.edu (CJL); tr9@st-andrews.ac.uk (TR); jon@astro.utoledo.edu (JEB); bwhitney@colorado.edu (BW)

© 2004 RAS

equilibrium. Our Monte Carlo radiation transfer technique naturally includes scattered light and the inclination dependence of the SED, which allows us to investigate the effects of highly flared discs. We construct synthetic spectral energy distributions and colours for discs of various sizes and masses surrounding brown dwarfs of various masses and luminosities. Our model SEDs enable us to determine to what extent observations in various spectral regions can diagnose disc parameters. The derivation of disc parameters for large numbers of sources may help in discriminating brown dwarf formation mechanisms and in determining whether they are different for dense and sparse star-forming regions.

The layout of the paper is as follows: Section 2 outlines the ingredients of our models and the radiation transfer/disc density calculation; Section 3 presents disc structure models derived with our iterative technique; Section 4 presents our model SEDs and colour–colour diagrams; Section 5 compares our models with currently available observations of brown dwarf discs; and Section 6 summarizes the results.

2 MODEL INGREDIENTS

This study implements a number of extensions to the original Monte Carlo radiative equilibrium technique of Bjorkman & Wood (2001). These include a crude estimate of the inner disc radius (assumed to be at the dust destruction radius) and an improved temperature structure calculation. Our discs are not vertically isothermal or two-layered (Natta & Testi 2001); 2D disc temperature structure is calculated in the Monte Carlo simulation based on the technique described by Lucy (1999). Our code self-consistently determines the density structure of a passively heated disc in vertical hydrostatic equilibrium. The extensions to the radiation transfer technique are described in greater detail in the Appendix.

2.1 Disc structure calculation

Model SEDs are computed for a flared disc that is heated by radiation from a central brown dwarf. We only consider passive discs, since disc heating from viscous accretion is negligible compared with stellar heating in low-accretion-rate systems (Muzerolle et al. 2000; D'Alessio et al. 1999). Our discs extend from the dust destruction radius to an outer radius of 100 au. The disc is truncated sharply at its inner edge and there is no material between the inner edge and the star, equivalent to assuming that material in this region is optically thin. In our previous modelling of CTTS SEDs (Wood et al. 2002a,b; Schneider et al. 2003; Grosso et al. 2003) we adopted the following flared disc density structure (e.g. Shakura & Sunyaev 1973):

$$\rho = \rho_0 \left(\frac{R_\star}{\varpi}\right)^\alpha \exp -\frac{1}{2}[z/h(\varpi)]^2, \tag{1}$$

where ϖ is the radial coordinate in the disc mid-plane, and the scaleheight increases with radius, $h = h_0(\varpi/R_\star)^\beta$. With the disc structure fixed we then calculate the temperature structure and emergent SED using the Monte Carlo radiative equilibrium technique of Bjorkman & Wood (2001).

In this paper we adopt an iterative scheme to determine the disc density structure. Having calculated the disc temperature structure via our Monte Carlo radiative equilibrium technique, we impose vertical hydrostatic equilibrium and solve

$$\frac{\mathrm{d}P}{\mathrm{d}z} = -\rho g_z. \tag{2}$$

Here, $P = \rho c_\mathrm{s}^2$ is the gas pressure, c_s is the isothermal sound speed, and $g_z = GM_\star z/\varpi^3$ is the vertical component of gravity in the disc. We make the usual thin-disc assumptions and assume that the disc is non-self-gravitating (Pringle 1981). We impose the boundary condition that the disc surface density $\Sigma \sim \varpi^{-1}$, in accordance with the detailed disc structure models of D'Alessio et al. (1999). Our simulations begin with the disc structure given by equation (1) with $\alpha = 2.25$, $\beta = 1.25$, and we iterate to derive a self-consistent vertical density structure. The density converges within three iterations.

In hydrostatic disc models, the disc scaleheight scales with radius as $h/\varpi = c_\mathrm{s}/v_\mathrm{c}$, where $c_\mathrm{s}^2 = kT/\mu m_\mathrm{H}$ and $v_\mathrm{c}^2 = GM_\star/\varpi$ are the isothermal sound speed and circular velocity at ϖ (e.g. Shakura & Sunyaev 1973; Lynden-Bell & Pringle 1974). For CTTS, h(100 au) is in the range 7 to 20 au, as found from radiative and hydrostatic equilibrium models (D'Alessio et al. 1999) and from fitting SEDs and scattered-light images of discs using equation (1) with h_0 as a free parameter (Burrows et al. 1996; Stapelfeldt et al. 1998; Grosso et al. 2003; Schneider et al. 2003). However, for discs around brown dwarfs the scaleheights may be larger due to the smaller circular velocity of these low-mass objects. If brown dwarf discs are indeed more vertically extended, then there may be a larger fraction of obscured brown dwarfs than of obscured CTTS. Our SED calculations enable us to address this issue.

2.2 Dust parameters and model atmospheres

The circumstellar dust opacity and scattering properties are taken to be those of the dust-size distribution we adopted for modelling the SEDs of HH 30 IRS and GM Aur (Wood et al. 2002a; Schneider et al. 2003; Rice et al. 2003). This dust model has a larger average grain size and a shallower wavelength-dependent opacity than ISM dust models (e.g. Mathis, Rumpl & Nordsieck 1977; Kim, Martin & Hendry 1994). There is much observational evidence for large grains and a shallow wavelength-dependent opacity in T Tauri discs (e.g. Beckwith et al. 1990; Beckwith & Sargent 1991; D'Alessio, Calvet & Hartmann 2000; Cotera et al. 2001; Wood et al. 2002a). The larger-grain dust model we adopt does not exhibit strong silicate features (see Wood et al. 2002a).

The input stellar spectra for the brown dwarf models are the BD˙Dusty model atmospheres presented by Allard et al. (2001), with $\log g = 3.5$ and effective temperatures of $T_\star = 2200$, 2600 and 2800 K. For CTTS models we use a 4000 K Kurucz model atmosphere (Kurucz 1994).

2.3 Parameter space

We construct radiative and hydrostatic equilibrium models for brown dwarf systems with the range of stellar and circumstellar disc parameters given in Table 1. The stellar mass range of $0.01\ \mathrm{M}_\odot \leqslant M_\star \leqslant 0.08\ \mathrm{M}_\odot$ covers objects from the hydrogen-burning limit down to the lower limit for brown dwarfs as identified via colour–magnitude diagrams by Muench et al. (2001). The corresponding stellar radii and temperatures yield models representative of 1-Myr old systems from the evolutionary tracks of Baraffe et al. (2002). For each set of stellar parameters, disc-to-star mass ratios of $\log(M_\mathrm{d}/M_\star) = -1$, -2 and -3 are initially considered. The disc mass M_d refers to the total disc mass of dust and gas. As with our previous work, this mass does not include very large particles such as rocks or planetesimals and is therefore a lower limit. We compare our resulting brown dwarf disc structures with those of discs around a typical CTTS with $M_\star = 0.5\ \mathrm{M}_\odot$, $R_\star = 2\ \mathrm{R}_\odot$, and $T_\star = 4000$ K (e.g. Kenyon & Hartmann 1995; D'Alessio et al. 1999).

Table 1. Model parameters.

$M_\star$ ($M_\odot$)	$T_\star$ (K)	$R_\star$ ($R_\odot$)	$L_\star$ ($L_\odot$)
0.01	2200	0.25	0.0013
0.04	2600	0.50	0.0038
0.08	2800	0.90	0.044

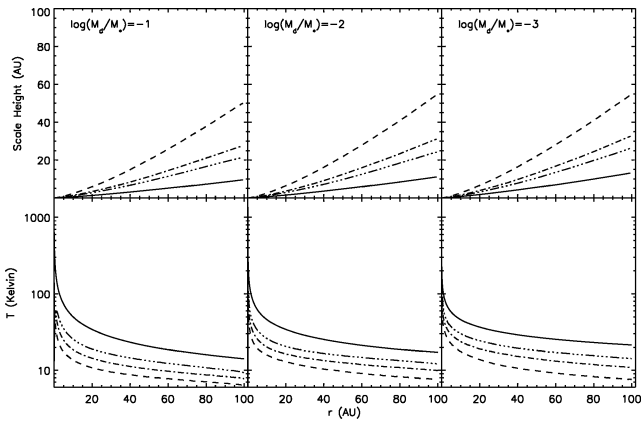

Figure 1. Upper: scaleheights of brown dwarf models compared with CTTS models with matching disc mass. Lower: mid-plane temperatures. In each plot the dashed, dot-dashed and triple-dot-dashed lines represent central stars of mass 0.01, 0.04 and 0.08 $M_\odot$ respectively, and the solid line represents the CTTS model. The disc-to-stellar mass ratio is indicated in each panel.

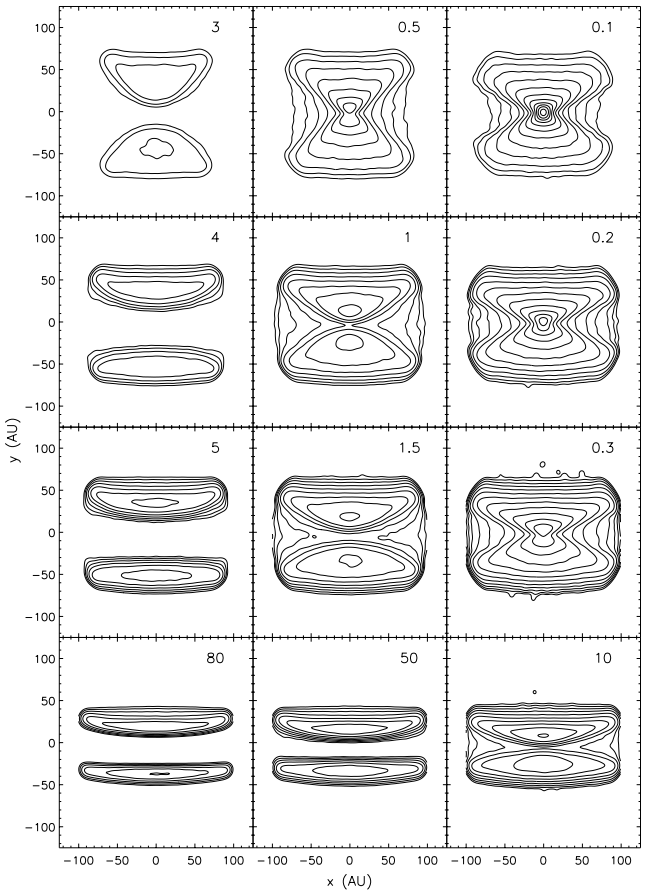

Figure 2. *K*-band contour plots of nine brown dwarf models and three comparison CTTS models. In declining order, each row represents models of stellar mass 0.01, 0.04 and 0.08 $M_\odot$, and the bottom row is the CTTS model. Moving from left to right each column represents models with $\log(M_d/M_\star) = -1$, -2 and -3. The number in each panel is the lowest contour level in μJy arcsec^{-2}, assuming the source is at 150 pc. Contours increase in 1 mag intervals.

3 DISC STRUCTURE MODELS

At the end of our iterative procedure (described in the Appendix) the outputs of our code are the disc density and temperature structure and the emergent SED. All our brown dwarf models have the Toomre parameter > 1 throughout their discs, so the thin-disc assumption implicit in our models is still valid (e.g. D'Alessio et al. 1999). Fig. 1 shows scaleheights and mid-plane temperatures for discs of various masses illuminated by stars of various masses. The full disc structure is now calculated; however, we choose to define scaleheight using the mid-plane temperature (see Appendix). For comparison we show the scaleheight and mid-plane temperature for a CTTS illuminating discs of the same mass ratio as in the brown dwarf models. The scaleheights of the CTTS discs are $h(100\ \mathrm{au}) \sim 15$ au, in agreement with the simulations of D'Alessio et al. (1999). The brown dwarf discs have scaleheights significantly in excess of those obtained for CTTS, with $h(100\ \mathrm{au})$ ranging from just over 20 au for $M_\star = 0.08\ M_\odot$ to almost 60 au for $M_\star = 0.01\ M_\odot$.

Our temperature calculations in Fig. 1 for brown dwarf discs show that $T\ (100\ \mathrm{au}) \sim 10$ K, with little variation among the models. It is therefore stellar mass that predominantly controls the disc scaleheights. The brown dwarf models show disc scaleheights up to three times larger than for comparable discs illuminated by a CTTS. Such large scaleheights will result in a large range of viewing angles for which direct starlight will be obscured by the disc. The effects of large scaleheights on the SED and colours are discussed in Section 4.

The extended nature of the brown dwarf discs is also clear in Fig. 2, which shows *K*-band scattered-light images of discs viewed at an inclination of 85° from face-on. As with CTTS models (Wood et al. 1998), the dust lane narrows with decreasing disc mass and the central source becomes increasingly more visible. Hence it seems that the detection of low-mass discs via scattered light may only be possible for edge-on systems or if coronographic techniques are used to block the starlight.

4 MODEL SPECTRA AND COLOURS

In addition to calculating the disc structure, our radiation transfer code outputs the SED for a range of viewing angles. This section gives SEDs and colour–colour diagrams that illustrate the main features of our models. With the Monte Carlo technique it is straightforward to determine the contributions to the SED of stellar, scattered, and thermally reprocessed photons (Wood et al. 2002a). We utilize this capability to determine the relative importance of the scattered-light contribution to the SEDs and colours.

4.1 SEDs of face-on discs

Our brown dwarf model SEDs have similar spectral characteristics to those of CTTS discs (e.g. Wood et al. 2002b). Fig. 3 shows SEDs of face-on discs for a range of star and disc parameters. Face-on covers 0° → 18° due to binning of the photons in the Monte Carlo code. The dependence of SED on disc mass is readily evident, and,

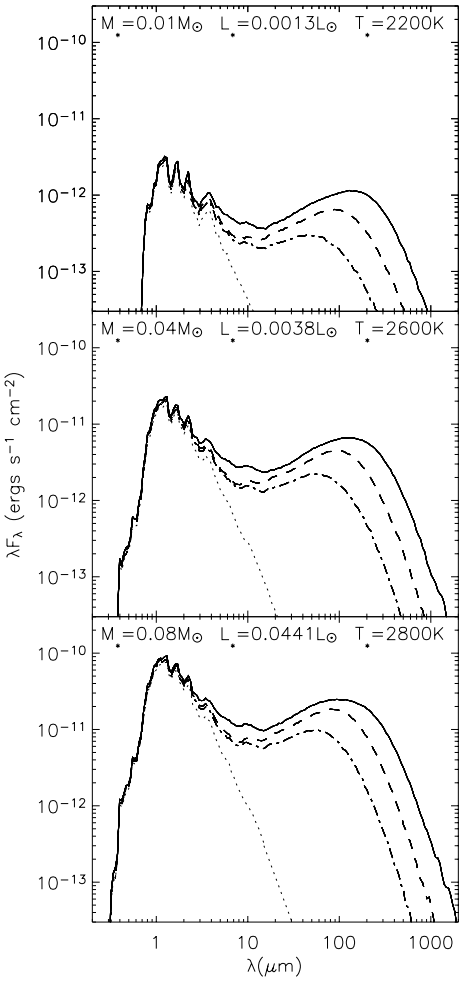

Figure 3. Face-on model SEDs showing the effects of varying stellar properties and disc mass. Each plot contains three separate SEDs for $\log(M_{\rm d}/M_\star) = -1$ (solid line), -2 (dashed line) and -3 (dot-dashed line). The dotted line represents the input stellar spectrum. Other parameters are as described in the text.

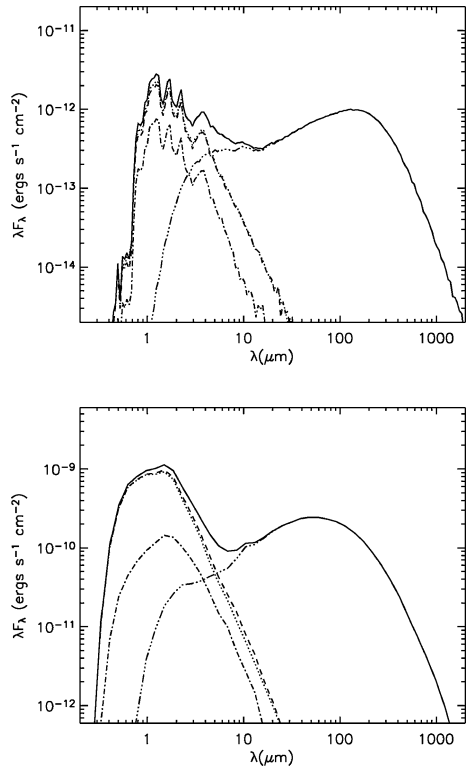

Figure 4. SEDs showing contributions from direct (dashed line), scattered (dot-dashed line) and disc-reprocessed photons (triple dot-dashed line) along with the input stellar spectrum (dotted line) and the total SED (solid line). Upper: brown dwarf model with $M_\star = 0.01$ M$_\odot$, $\log(M_{\rm d}/M_\star) = -1$ and $L_\star = 0.0013$ L$_\odot$. Lower: CTTS model with $\log(M_{\rm d}/M_\star) = -1$.

as with CTTS, observations at long wavelengths provide the best diagnostics of disc mass.

As noted by Natta & Testi (2001), it is difficult to produce significant near-IR excesses for brown dwarfs because the stellar spectrum peaks at longer wavelengths than for CTTS and can therefore dominate the disc thermal emission. At longer wavelengths, however, Fig. 3 shows that our brown dwarf models are capable of producing varying degrees of IR excess emission. As stellar mass decreases, scaleheights increase, allowing the disc to intercept, scatter, and thermally reprocess more stellar radiation, which in turn gives rise to increasingly large IR excesses.

Fig. 4 shows the relative contribution of stellar, scattered, and thermal disc radiation for the highly flared $M_\star = 0.01$ M$_\odot$, $T_\star =$ 2200 K brown dwarf disc system with $\log(M_{\rm d}/M_\star) = -1$, and includes a CTTS model for comparison. Scattered light makes little contribution to face-on models, but it can account for up to 90 per cent of K-band flux as discs become more inclined (see Wood et al. 2002b, their fig. 9). The importance of including scattered light will be highlighted in Section 4.3.

Recent work on brown dwarf formation suggests that many brown dwarfs are ejected from multiple systems and that any circumstellar discs that survive the ejection will be very small. In the numerical simulations of Bate, Bonnell & Bromm (2003), no discs survive around ejected brown dwarfs down to their simulation resolution of ∼10 au. We have computed SEDs for discs of constant mass, but varying $R_{\rm d}$ in the range 10–200 au. Because $M_{\rm d}$ was held constant in these models, smaller $R_{\rm d}$ yields larger optical depths. The SEDs are mostly unaltered as $R_{\rm d}$ changes, apart from some variation at far-IR/submm wavelengths. We conclude that it is very difficult to determine disc radii from SED data alone, and more stringent tests of the small-disc prediction of Bate et al. (2003) will require high-resolution imaging to resolve the discs via their scattered light and thermal emission (see also, Beckwith et al. 1990; Chiang et al. 2001).

4.2 Near-IR colour–colour diagrams

By far the most popular technique for identifying circumstellar discs is to identify sources with near-IR excess emission in colour–colour diagrams (e.g. Lada & Adams 1992; Rebull et al. 2002). It was through near-IR colour–magnitude and colour–colour diagrams that Muench et al. (2001) and Liu et al. (2003) identified many candidate brown dwarfs that exhibit the tell-tale IR excess emission indicative of circumstellar discs.

All colours we present are relative to Vega and are computed using 2MASS *JHK* and UKIRT *L* filter transparency curves. The BD˙Dusty model atmospheres that we use have near-IR colours that are bluer than observations of the corresponding spectral type (e.g. Bessell & Brett 1988; Kirkpatrick et al. 2000). What is

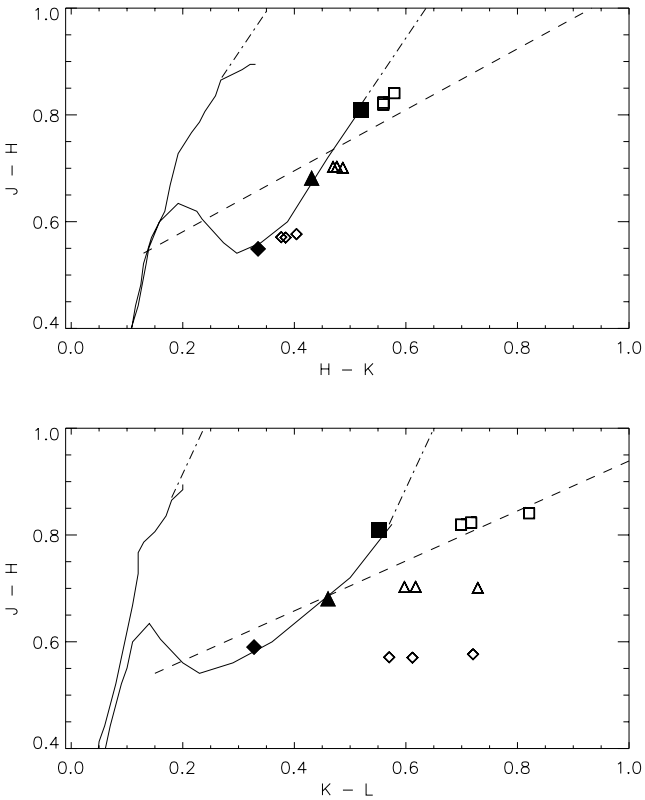

Figure 5. *JHKL* colour–colour diagrams containing face-on colours for brown dwarf models with various $T_\star$, M_d and $M_\star$. The reddest colours correspond to low stellar masses and therefore highly flared discs. The filled symbols of corresponding shape represent the average stellar colour of all models at fixed temperatures of 2200, 2600 and 2800 K. The CTTS locus (dashed line) is taken from Meyer et al. (1997). The giant branch and M dwarf locus (solid lines) are taken from Bessell & Brett (1988) and Kirkpatrick et al. (2000). The dot-dashed lines represent reddening vectors. Models have been shifted so that average stellar colours lie on the 'brown dwarf locus'.

important is the relative colour of our models (e.g. $[H-K]-[H-K]_\star$), and the underlying stellar spectrum does not affect this. As we ultimately compare our models with observations, we have used a similar approach to Liu et al. (2003) and applied a colour offset to the models so that the model stellar colours match observations. We adopt spectral types of M9.5, M8.5 and M6 for our 2200, 2400 and 2800 K models respectively. There is no well-defined temperature scale for M dwarfs and so classifications were chosen on consideration of observations and discussion by Luhman (1999), Pavlenko, Zapatero Osorio & Rebolo (2000) and Dahn et al. (2002). We shift the stellar colours of our models to match the field M dwarf locus taken from Bessell & Brett (1988) and average colours from Kirkpatrick et al. (2000). This results in the following offsets for the M9.5, M8.5 and M6 fits: $\Delta(J-H) = 0.34, 0.23, 0.10$, $\Delta(H-K) = 0.12, 0.06, 0.00$. No shift in $K-L$ is applied.

Fig. 5 shows *JHK* and *JHKL* colour–colour diagrams for our model discs viewed face-on, and following the aforementioned adjustments. In general, excess emission is more readily detected at long wavelengths (e.g. Haisch, Lada & Lada 2000; Natta & Testi 2001) and this is again seen here with models showing larger excesses at $K-L$ than at $J-H$ or $H-K$. The trend of our models is that the more massive and more flared discs exhibit the largest IR excesses. Inclination effects yield a spread in colour–colour diagrams and we explore this in the next section.

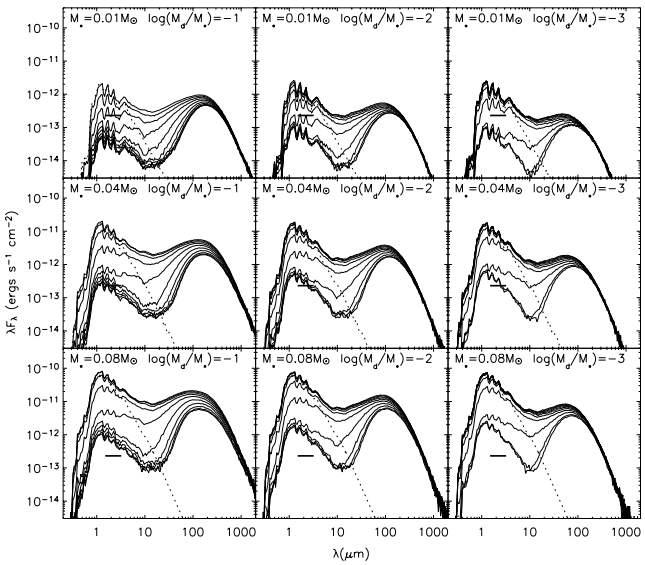

Figure 6. SEDs illustrating obscured fractions for our grid of brown dwarf models. Obscured fractions range from 20 up to 60 per cent, whereas comparable CTTS models show 20 per cent. The greatest obscuration in a brown dwarf model occurs for the lowest stellar mass of $M_\star = 0.01$ M$_\odot$, with $\log(M_\mathrm{d}/M_\star) = -1$ and $T_\star = 2200$ K, $L_\star = 0.0013$ L$_\odot$. Least obscuration occurs for the highest stellar mass of $M_\star = 0.08$ M$_\odot$, with $\log(M_\mathrm{d}/M_\star) = -3$ and $T_\star = 2800$ K, $L_\star = 0.044$ L$_\odot$. The thick horizontal solid line represents a detection limit of 16.5 mag at K.

4.3 Inclination, scattered light and obscured fractions

For highly inclined CTTS, direct starlight is blocked by the optically thick disc and such systems will be very faint in the optical and near-IR (e.g. D'Alessio et al. 1999; Wood et al. 2002a,b). Compared to CTTS, the larger disc scaleheights we derive for the brown dwarf models will result in a larger fraction of viewing angles over which the central starlight is blocked by the disc. For the purpose of this study we define an 'obscured source' to be one for which the near-IR flux is at least 3 mag fainter than the corresponding face-on source. The obscured fraction therefore depends on the disc size, mass, and scaleheight. For CTTS, the obscured fraction is around 20 per cent (D'Alessio et al. 1999; Wood et al. 2002b) for discs of $M_\mathrm{d} \sim 10^{-3}$ M$_\odot$.

Fig. 6 shows the inclination effect on the SEDs for various brown dwarf disc models. The SEDs are shown for 10 viewing angles evenly spaced in cos i, so that each curve represents 10 per cent of sources by number if we assume that sources are randomly distributed in inclination angle. We find obscured fractions from 20 to 60 per cent, with highly inclined sources only detected in the near-IR via scattered light and weak thermal emission. The largest obscured fraction occurs for the lowest stellar mass of $M_\star = 0.01$ M$_\odot$ with $\log(M_\mathrm{d}/M_\star) = -1$ and $T_\star = 2200$ K. The smallest obscured fraction occurs for the highest stellar mass of $M_\star = 0.08$ M$_\odot$ with $\log(M_\mathrm{d}/M_\star) = -3$ and $T_\star = 2800$ K.

Studies of the initial mass function in Trapezium, ρ Ophiucus and IC348 show a relatively flat distribution over the range $0.08 \leqslant M_\star$ (M$_\odot$) $\leqslant 0.04$ and then a sharp fall-off below this (Luhman 2000; Muench et al. 2002). If the IMF is flat and the fall-off due to small number statistics then within a young cluster population up to 55 per cent of brown dwarf candidates, as defined by our parameter range, may be obscured. This is an upper limit produced using maximum obscuration fractions for each stellar mass assuming a disc-to-stellar

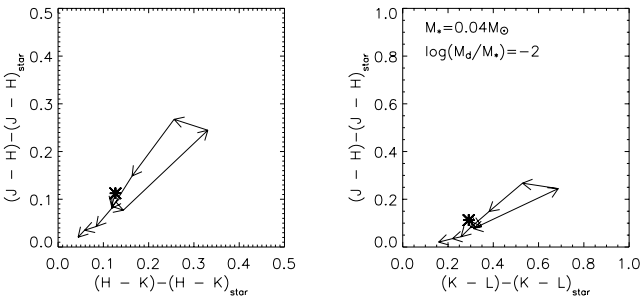

Figure 7. *JHKL* plot for the $M_\star = 0.04\ \mathrm{M}_\odot$ and $\log(M_\mathrm{d}/M_\star) = -2$ brown dwarf model. Arrows indicate the change in colours as inclination varies from nearly edge-on (indicated by bold asterisk) to face-on, and colours are relative to the central star's colours. This plot is indicative of the behaviour of all the brown dwarf models.

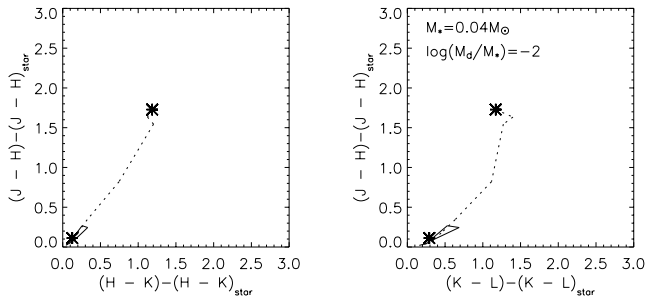

Figure 8. *JHKL* plots as in Fig. 7, but with dotted lines showing the change at each inclination that would result if scattering effects were removed.

mass ratio of $\log(M_\mathrm{d}/M_\star) = -1$. For a declining IMF, and a distribution of disc masses, the obscured fraction will be lower. Within our parameter range a minimum of 20 per cent of sources are likely to be obscured regardless of stellar mass distribution and assuming disc-to-stellar mass ratios of $\log(M_\mathrm{d}/M_\star) = -3$.

The relatively low luminosity of brown dwarfs and the increased obscuration due to highly flared discs may result in detection problems. At a distance of 150 pc (as used in Fig. 6) it would be possible to detect some obscured sources in the *K* band assuming a sensitivity limit of 16.5 mag. In the absence of high-resolution imaging, however, these sources may be incorrectly identified as low-luminosity systems. A three-fold increase in distance would be sufficient to make all obscured sources undetectable at this sensitivity limit.

Fig. 7 shows the inclination dependence in the brown dwarf *JHKL* colour–colour diagrams. Relative colours are plotted for 10 inclinations, with the change in colour at each inclination indicated by an arrow. Similar to the behaviour observed by Kenyon et al. (1993) and Whitney, Kenyon & Gomez (1997), we see a loop in the colour–colour plane with inclination. Starting from face-on, the sources generally become redder with increasing inclination and then loop around and end up with edge-on sources being slightly bluer than face-on ones, but still redder than the intrinsic stellar colours. Edge-on sources are seen almost entirely via scattered light. Note that these are slightly redder than the star because the scattered light, which is relatively blue, suffers extinction and becomes reddened. This trend is seen in all of the models.

Fig. 8 contains data for the same model as in Fig. 7, but also shows the change in colour with inclination if scattered light is ignored. The removal of scattered light makes the colours much redder, with the effect being particularly significant at moderate to high inclinations. This emphasizes the importance of including scattering when creating and studying models of such systems.

4.4 CTTS/brown dwarf confusion

When only unresolved photometry is available, our models show that edge-on CTTS could be mistaken for brown dwarfs. CTTS have edge-on flux levels that are comparable to those for face-on brown dwarfs and similar colours. Muench et al. (2001) identified sources within the Trapezium cluster with $13.5 \lesssim H \lesssim 17.5$ as candidate brown dwarfs. They note that 21 of their 109 brown dwarf candidates are coincident with optically resolved proplyds (Bally, O'Dell & McCaughrean 2000; O'Dell & Wong 1996), and 21 per cent of the candidates that exhibit IR excess, indicative of circumstellar discs, are represented by these proplyds. In the absence of high-resolution imaging, the task of identifying faint sources such as brown dwarfs may be problematic. If no central star is seen then these sources could be edge-on CTTS that happen to have the same magnitude and colours as a pole-on brown dwarf and disc. This confusion could lead to an overestimation of brown dwarf numbers.

5 COMPARISON WITH OBSERVATIONS

This section compares our synthetic models with published observations of suspected brown dwarf discs. For the Chameleon cluster, the SED data are taken from Comerón et al. (2000) and Apai et al. (2002); ρ Ophiucus data come from Barsony et al. (1997), Comerón et al. (1998), Bontemps et al. (2001) and Natta et al. (2002). *JHKL* data are taken from the above papers along with Kirkpatrick et al. (2000) and Liu et al. (2003). All near-IR photometry has been converted to the 2MASS system (Carpenter 2001).

5.1 Spectral energy distributions

Fig. 9 shows flared disc model fits to the SED data for candidate brown dwarfs in the ρ Ophiucus and Chameleon star clusters. Table 2 contains details of the model parameters used to produce the fits. We used stellar parameters from Natta & Testi (2001) and Natta et al. (2002) as starting points for each of our models.

Natta & Testi (2001) modelled Cha Hα 1, 2 and 9 using a flared disc model. Their models produced a successful fit in the mid-IR region of the spectrum and predicted a strong 10-μm silicate emission feature. Apai et al. (2002) later made observations of Cha Hα 2 at 9.8 and 11.9 μm and did not detect the silicate feature. They presented an optically thick flat disc model which produced no silicate feature. The SEDs of ρ Oph sources have been modelled by Natta et al. (2002), and they found indications that as many as eight of these stars may have flat discs.

Our models open up the possibility that the absence of a silicate feature may be explained with larger circumstellar dust grains. In addition, low-mass discs may fit SEDs previously modelled with flat discs. As Fig. 9 demonstrates, it is possible to fit the observed data for all sources with a flared disc geometry. The use of larger grains naturally suppresses the silicate feature that has been shown to be missing from the Chameleon data, and low-mass discs of $10^{-5}\ \mathrm{M}_\odot$ and $10^{-7}\ \mathrm{M}_\odot$ allow us to fit the IR data of the candidates where flat discs were previously suspected. We note that many of these fits have disc-to-stellar mass ratios outside the typical range of $-1 \leqslant \log(M_\mathrm{d}/M_\star) \leqslant -3$ (Natta, Grinin & Mannings 2000; Klein et al. 2003), and flat discs (Natta et al. 2002) remain a possibility.

Another possibility, testable with long-wavelength observations, is that steeper surface density profiles can be used to fit the data with higher-mass discs. In Fig. 10, ISO#030 has been modelled

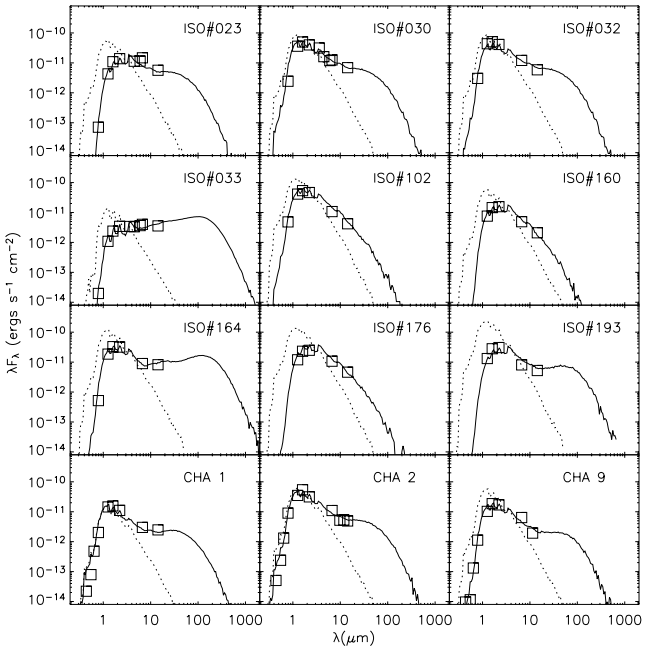

Figure 9. Model SED fits to observed data in ρ Ophiucus and Chameleon star clusters as indicated. All models are of a flared disc around a central star with an inner gap of radius $2R_\star$. A distance of 150 pc is assumed for both clusters. Further model parameters are given in Table. 2. The dotted line represents the input spectrum. For ISO#030 two models are presented. In all cases a solid line indicates surface density $\Sigma \sim \varpi^{-1}$. For ISO#030 the dashed line indicates $\Sigma \sim \varpi^{-2}$. The data are not corrected for the effects of reddening; instead, the models are reddened according to Cardelli, Clayton & Mathis (1989) with exctinction parameter $R_v = 4$.

Table 2. Model fit parameters.

Object	$T_\star$ (K)	$R_\star$ ($R_\odot$)	$M_\star$ ($M_\odot$)	M_d ($M_\odot$)	A_v (mag)	Inclination (°)
ISO#023	2600	0.95	0.04	10^{-5}	8	0
ISO#030	2600	1.2	0.08	10^{-5}	2	0
ISO#032	2600	1.2	0.08	10^{-5}	3	0
ISO#033	2200	0.63	0.01	10^{-3}	7	0
ISO#102	3000	1.17	0.08	10^{-7}	3.5	0
ISO#160	2600	0.95	0.08	10^{-7}	6	0
ISO#164	2600	1.36	0.08	10^{-3}	4	63
ISO#176	3000	1.17	0.08	10^{-7}	7	60
ISO#193	3000	1.5	0.08	10^{-5}	7	78
CHA Hα1	2600	0.5	0.01	10^{-5}	0.3	0
CHA Hα2	2600	1.05	0.04	10^{-5}	1.1	37
CHA Hα9	2600	0.95	0.08	10^{-5}	3.2	72

using both surface density $\Sigma \sim \varpi^{-1}$ and $\Sigma \sim \varpi^{-2}$. The use of $\Sigma \sim \varpi^{-2}$ allows the data to be fitted with a disc eight times more massive than that used in the $\Sigma \sim \varpi^{-1}$ case. Both models fit the data well in the near-IR/mid-IR, but are quite different in the far-IR. Long-wavelength observations would help to discriminate between flat disc, low-mass flared disc, and steeper surface density disc models.

If lower-mass flared models are representative of discs in brown dwarf populations, as opposed to higher-mass discs, then problems with obscuration may not be as significant as suggested in Section 4.3. Equally, flat discs do not result in severe obscuration of the central star unless at very high inclinations.

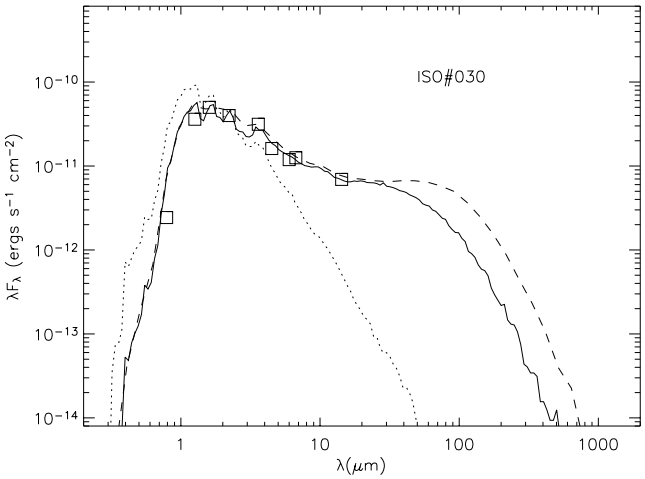

Figure 10. Model SED fits as in Fig. 9. Two models are presented for ISO#030. The solid line indicates surface density $\Sigma \sim \varpi^{-1}$. The dashed line indicates $\Sigma \sim \varpi^{-2}$. Model parameters for the $\Sigma \sim \varpi^{-1}$ case are given in Table 2. The $\Sigma \sim \varpi^{-2}$ model has a disc eight time more massive.

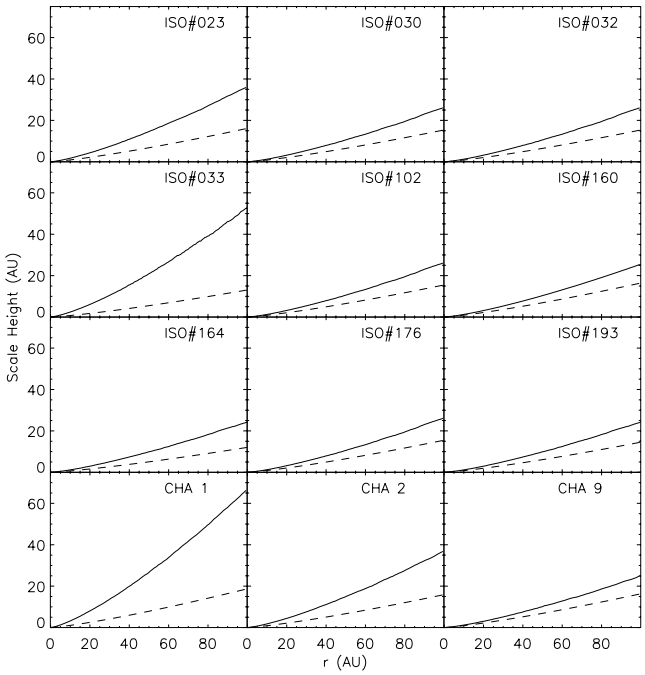

Figure 11. Scaleheights for our models (solid lines) presented in Fig. 9. The scaleheight for our 'typical CTTS' at matching disc-to-stellar mass ratio is given as a comparison (dashed line). For ISO#030 scaleheights are virtually coincident for the two models presented in Fig. 10, and therefore only the $\Sigma \sim \varpi^{-1}$ case is shown here.

Fig. 11 shows the derived scaleheights for the discs that we used to model the observed SEDs of Figs 9 and 10. This illustrates the range of disc structures that can produce fits to the observed data. In each plot the scaleheight of a model CTTS of corresponding disc-to-stellar mass ratio is presented as a comparison. For these models we find scaleheights up to three times that of the corresponding CTTS.

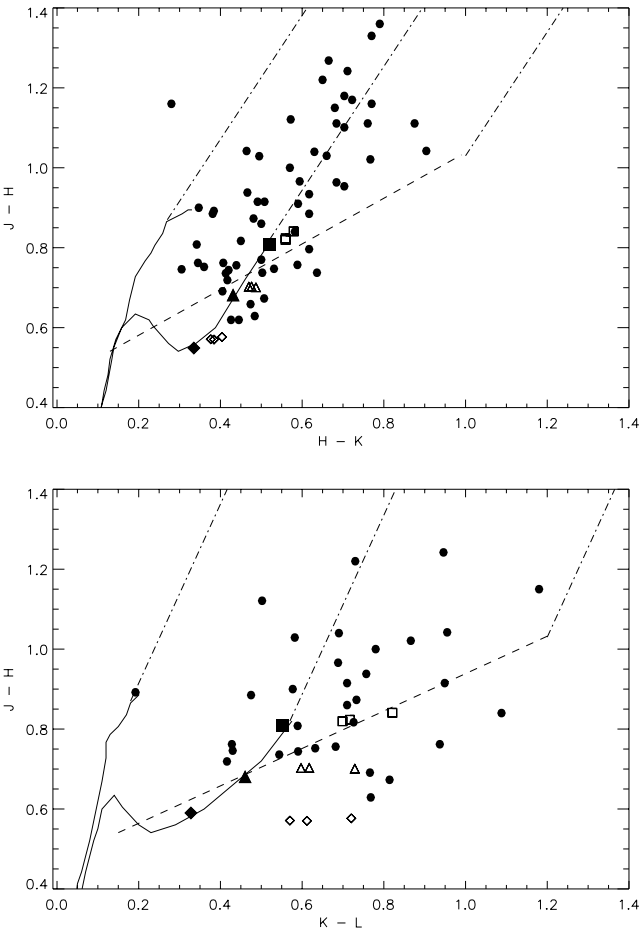

Figure 12. *JHKL* plots containing observed (•) and face-on model (square, triangle, diamond) colours. Where possible, data were obtained directly from the 2MASS second incremental data release (Carpenter 2001). Remaining data were retrieved from the papers of Comerón et al. (1998, 2000), Martín et al. (2001), Briceño et al. (1998), Luhman et al. (1998), Luhman (1999), Najita, Tiede & Carr (2000) and Liu et al. (2003). As previously, the solid shapes represent the average stellar colour obtained for models of $T_\star =$ 2200, 2600 and 2800 K. The CTTS locus (dashed line) is taken from Meyer et al. (1997). The giant branch and M dwarf locus (solid lines) are taken from Bessell & Brett (1988) and Kirkpatrick et al. (2000). The dot-dashed lines represent reddening vectors. Models have been shifted so that stellar colours lie on the 'brown dwarf locus'.

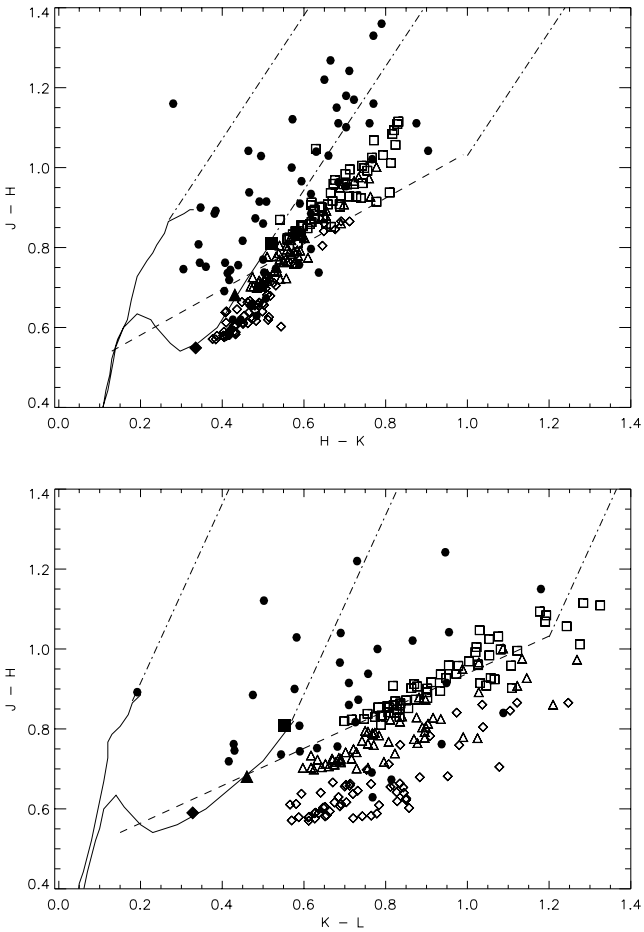

Figure 13. *JHKL* plots as in Fig. 12, but with model colours for all inclinations.

5.2 *JHKL* colours

Fig. 12 shows *JHKL* plots of our face-on models and published data. Following the adjustments discussed in Section 4.2, Fig. 11 shows that our models (if reddening were included) can reproduce the observed spread in colours of suspected brown dwarf disc systems. The inclusion of all inclinations (Fig. 13) allows for the redder colours of inclined discs and produces a spread in the *JHKL* plots that is in very good agreement with the observed colours.

Fig. 13 also shows the CTTS locus taken from Meyer, Calvet & Hillenbrand (1997). This again demonstrates that there is an overlap between CTTS and brown dwarf colours which may lead to incorrect identification of sources if only colour–magnitude data are available.

6 CONCLUSION

We have presented model SEDs and colour–colour diagrams for brown dwarf discs. The main assumptions in our models are that the discs are in vertical hydrostatic equilibrium with dust and gas well mixed throughout. Our models are self-consistent and employ an iterative procedure to determine the hydrostatic density structure for passively heated discs. Compared with CTTS, brown dwarf discs have larger scaleheights due to the lower mass of the central star. In some cases the scaleheights of brown dwarf discs are more than three times larger than for the same disc-to-stellar mass ratio for a CTTS. The larger scaleheights result in more inclinations over which the direct stellar radiation is blocked or obscured by the flared disc. The fraction of 'optically' obscured systems depends on the stellar mass and disc optical depth, and in our models is in the range 20 per cent $\leqslant f_{\rm obs}$ (2.2 μm) $\leqslant$ 60 per cent. For a typical CTTS about 20 per cent of sources will be obscured.

If, as our models suggest, brown dwarf discs are highly flared, detection of brown dwarf disc systems will be biased towards face-on systems. We also show that, without direct imaging or spectroscopic identification, it will be difficult to distinguish between edge-on CTTS and face-on brown dwarfs. Colour–colour diagrams show that edge-on sources, which are only detected in the optical/near-IR via scattered light, have similar colours to face-on sources. This may lead to incorrect identification of sources. In particular, we find that an edge-on CTTS will have similar near-IR magnitudes and colours to face-on brown dwarf disc systems.

We compare our synthetic models to SED and colour–colour observations of suspected brown dwarfs and show that flared discs of varying mass can account for the observed SEDs and colours. Our

adopted circumstellar dust model naturally suppresses the 10-μm silicate feature that is absent in the observations of Cha Hα2. Long-wavelength observations are required to discriminate between our flared disc models and alternative flat disc models that have been proposed for some sources.

ACKNOWLEDGMENTS

We acknowledge financial support from a UK PPARC Studentship (CW); UK PPARC Advanced Fellowship (KW); NASA's Long Term Space Astrophysics Research Program, NAG5 8412 (BW), NAG5 8794 (JEB); and the National Science Foundation, AST 9909966 (BW), AST 9819928 (JEB).

REFERENCES

Allard F., Hauschildt P. H., Alexander D. R., Tamanai A., Schweitzer A., 2001, ApJ, 556, 357
Apai D., Pascucci I., Henning, Th., Sterzik M. F., Klein R., Semenov D., Gunther E., Sterzik B., 2002, ApJ, 573, L115
Bally J., O'Dell C. R., McCaughrean M. J., 2000, AJ, 119, 2919
Baraffe I., Chabrier G., Allard F., Hauschildt P. H., 2002, A&A, 382, 563
Barsony M., Kenyon S. J., Lada E. A., Teuban P. J., 1997, ApJS, 112, 109
Bate M. R., Bonnell I. A., Bromm V., 2003, MNRAS, 339, 577
Beckwith S. V. W., Sargent A. I., 1991, ApJ, 381, 205
Beckwith S. V. W., Sargent A. I., Chini R. S., Guesten R., 1990, AJ, 99, 924
Bessell M. S., Brett J. M., 1988, PASP, 100, 1134
Bjorkman J. E., Wood K., 2001, ApJ, 554, 615
Bontemps S. et al., 2001, A&A, 372, 173
Briceño C., Hartmann L., Stauffer J., Martín E., 1998, AJ, 115, 2074
Burrows C. J. et al., 1996, ApJ, 473, 437
Cardelli J. A., Clayton G. C., Mathis J. S., 1989, ApJ, 345, 245
Carpenter J. M., 2001, AJ, 121, 2851
Chiang E. I., Joung M. K., Creech-Eakman M. J., Qi C., Kessler J. E., Blake G. A., van Dishoeck E. F., 2001, ApJ, 547, 1077
Comerón F., Rieke G. H., Claes P., Torra J., Laureijs R. J., 1998, A&A, 335, 522
Comerón F., Neuhauser R., Kaas A. A., 2000, A&A, 359, 269
Cotera A. S. et al., 2001, ApJ, 556, 958
Dahn C. C. et al., 2002, AJ, 124, 1170
D'Alessio P., Cantó, J., Hartmann L., Calvet N., Lizano S., 1999, ApJ, 511, 896
D'Alessio P., Calvet N., Hartmann L., 2000, A&AS, 196, 408
Grosso N., Alves J., Wood K., Neuhäuser R., Montmerle T., Bjorkman J. E., 2003, ApJ, 586, 296
Haisch K. E., Jr, Lada E. A., Lada C. J., 2000, AJ, 120, 1396
Kenyon S. J., Hartmann L., 1987, ApJ, 323, 714
Kenyon S. J., Hartmann L., 1995, ApJS, 101, 117
Kenyon S. J., Whitney B. A., Gómez M., Hartmann L., 1993, ApJ, 414, 773
Kim S.-H., Martin P. G., Hendry P. D., 1994, ApJ, 422, 164
Kirkpatrick J. D. et al., 2000, AJ, 120, 447
Klein R., Apai D., Pascucci I., Henning Th., Waters L. B. F. M., 2003, ApJ, 593, L57
Kurucz R. L., 1994, CD-ROM 19, Solar Abundance Model Atmospheres
Lada C. J., Adams F. C., 1992, ApJ, 393, 278
Liu M. C., Najita J., Tokunaga A. T., 2003, ApJ, 585, 372
Lucy L. B., 1999, A&A, 344, 282
Luhman K. L., 1999, ApJ, 525, 466
Luhman K. L., 2000, ApJ, 544, 1044
Luhman K. L., Briceño C., Rieke G. H., Hartmann L., 1998, ApJ, 493, 909
Lynden-Bell D., Pringle J. E., 1974, MNRAS, 168, 603
Martín E. L., Dougados C., Magnier, E., Ménard F., Magazzú, A., Cuillandre J. -C., Delfosse X., 2001, ApJ, 561, L195
Mathis J. S., Rumpl W., Nordsieck K. H., 1977, 217, 425
Meyer M. R., Calvet N., Hillenbrand L. A., 1997, AJ, 114, 288
Muench A. A., Alves J., Lada C. J., Lada E. A., 2001, ApJ, 558, 51
Muench A. A., Lada E. A., Lada C. J., Alves J., 2002, ApJ, 573, 366 (Paper I)
Muzerolle J., Briceño C., Calvet N., Hartmann L., Hillenbrand L., Gullbring E., 2000, ApJ, 545, L141
Najita J. R., Tiede G. P., Carr J. S., 2000, ApJ, 541, 977
Natta A., Testi L., 2001, A&A, 376, L22
Natta A., Grinin V. P., Mannings V., 2000, in Mannings V., Boss A., Russell S. S., eds, Protostars and Planets IV. Univ. Arizona Press, Tucson, p. 559
Natta A., Testi L., Comern F., Oliva E., D'Antona F., Baffa C., Comoretto G., Gennari S., 2002, A&A, 393, 597
Oasa Y., Tamura M., Sugitani K., 1999, ApJ, 526, 336
O'Dell C. R., Wong K., 1996, AJ, 111, 846
Pavlenko Y., Zapatero Osorio M. R., Rebolo R., 2000, A&A, 355, 245
Pringle J. E., 1981, ARA&A, 19, 137
Rebull L. M. et al., 2002, AJ, 123, 1528
Reipurth B., Clarke C., 2001, AJ, 122, 432
Rice W. K. M., Wood K., Armitage P. J., Whitney B. A., Bjorkman J. E., 2003, MNRAS, 342, 79
Schneider G., Wood K., Silverstone M. D., Hines D. C., Koerner D. W., Whitney B. A., Bjorkman J. E., Lowrance P. J., 2003, AJ, 125, 1467
Shakura N. I., Sunyaev R. A., 1973, A&A, 24, 337
Shu F. H., Adams F. C., Lizano S., 1987, ARA&A, 25, 23
Stapelfeldt K. R., Krist J. E., Menard F., Bouvier J., Padgett D. L., Burrows C. J., 1998, ApJ, 502, L65
Testi L., Natta A., Oliva E., D'Antona F., Comeron F., Baffa C., Comoretto G., Gennari S., 2002, ApJ, 571, L155
Whitney B. A., Hartmann L., 1992, ApJ, 395, 529
Whitney B. A., Wolff M. J., 2002, ApJ, 574, 205
Whitney B. A., Kenyon S. J., Gomez M., 1997, ApJ, 485, 703
Wood K., Kenyon S. J., Whitney B., Turnbull M., 1998, ApJ, 497, 404
Wood K., Wolff M. J., Bjorkman J. E., Whitney B. A., 2002a, ApJ, 564, 887
Wood K., Lada C. J., Bjorkman J. E., Kenyon S. J., Whitney B., Wolff M. J., 2002b, ApJ, 567, 1183

APPENDIX A: MONTE CARLO RADIATION TRANSFER CODE DEVELOPMENTS

A1 Density structure

In this study we determine the structure of circumstellar discs based on the assumption that the disc is in vertical hydrostatic equilibrium with dust and gas well mixed. We therefore solve the hydrostatic equilibrium equation

$$\frac{\mathrm{d}P}{\mathrm{d}z} = -\rho g_z, \tag{A1}$$

where P is the pressure, ρ is the density, and g_z is the vertical component of gravity in the disc. Conservation of mass in the disc is enforced by keeping the radial dependence of the surface density.

The hydrostatic equation has an analytic solution if the disc temperature is assumed to be vertically isothermal at any given cylindrical radius, ϖ. Using the mid-plane temperature, $T(\varpi)$, the disc density has a Gaussian distribution about the mid-plane with scaleheight

$$h(\varpi) = \left(\frac{kT(\varpi)\varpi^3}{GM_\star \mu m_\mathrm{H}}\right)^{\frac{1}{2}}, \tag{A2}$$

where k and G are the Boltzmann and Newton constants, m_H is the mass of hydrogen and μ is the molecular weight of disc material and is taken to be $\mu = 2.3$ for a molecular hydrogen/helium combination.

In order to solve for the density numerically, we approximate the integral of equation (A1) to a sum of finite contributions. Using the equation of state, $P = \rho c_s^2$, where $c_s^2 = kT/\mu m_H$ is the local sound speed squared, this leads to

$$\ln\left(\frac{\rho}{\rho_0}\right) = -\sum \frac{1}{T}\left(\frac{dT}{dz} + \frac{g_z \mu m_H}{k}\right)\Delta z, \tag{A3}$$

which can be solved using

$$\frac{dT}{dz} = \cos\theta \frac{dT}{dr} - \frac{\sin\theta}{r}\frac{dT}{d\theta}. \tag{A4}$$

In the discretization of the disc density we use a spherical polar grid (Whitney & Wolff 2002) throughout which we calculate g_z at the mid-point of each cell. The cell temperature determined from our radiative equilibrium calculation is assumed to be uniform within each cell, and Δz is the incremental distance through each cell that lies directly below grid centre (r, θ, ϕ). It is therefore possible to obtain values of ρ/ρ_0 for each grid cell.

We assume that the disc surface density has the form $\Sigma(r) = \Sigma_0(\varpi/R)^{-1}$, which agrees with the disc structure models of D'Alessio et al. (1999). Since the total disc mass is given by

$$M_d = \int_{Rmin}^{Rmax} \Sigma(\varpi) 2\pi\varpi \, d\varpi, \tag{A5}$$

we can solve for Σ_0 and in turn obtain $\Sigma(\varpi)$. We then normalize ρ_0 so that the surface density is a constant,

$$\rho_0(\varpi) = \frac{\Sigma_0(R/\varpi)}{\sum \rho/\rho_0 \Delta z}. \tag{A6}$$

For each cell ρ/ρ_0 and the cylindrical radius, ϖ, are known, so we may therefore determine the density in each cell.

A2 Temperature structure

In order to determine the density structure we require an accurate calculation of the disc temperature structure. While the Bjorkman & Wood (2001) technique yields accurate SEDs, we found that the temperature calculation was too noisy for use in our density calculation. Increasing the number of photon energy packets yields a smoother temperature structure at the cost of a large increase in CPU time. We have therefore implemented the temperature calculation technique of Lucy (1999), which is based on using an estimator for the mean intensity of the radiation field. Integrating this technique into our Monte Carlo code leads to a higher signal-to-noise ratio in the disc temperature determination with fewer photon packets. What follows is an outline of the procedure we use, and we refer the reader to Lucy (1999) for more details.

Provided a system is in radiative equilibrium, the rate at which matter absorbs energy from the radiation field is balanced by the rate at which matter emits energy, $\dot{A} = \dot{E}$, or,

$$4\pi \int_0^\infty \rho(1 - a_\nu)\kappa_\nu J_\nu \, d\nu = 4\pi \int_0^\infty \rho(1 - a_\nu)\kappa_\nu B_\nu \, d\nu. \tag{A7}$$

As discussed by Lucy (1999) the mean intensity, J_ν, and therefore heating, is proportional to the photon path-lengths, l, through the cells, yielding

$$\dot{A} = \frac{\epsilon}{\delta t \delta V} \sum l\rho(1 - a_\nu)\kappa_\nu, \tag{A8}$$

where δt is the cell simulation time, δV is the cell volume, a_ν is the scattering albedo, and κ_ν is the total opacity in $cm^2\,g^{-1}$. The energy of each photon packet is $\epsilon = L\delta t/N$, where L is the source luminosity and N is the number of Monte Carlo photon packets used in our simulation. The expression for the rate at which matter emits energy can also be simplified, to

$$\dot{E} = 4\pi\rho\kappa_P B(T), \tag{A9}$$

where κ_P is the Planck mean absorption coefficient and $B(T) = \sigma\, T^4/\pi$ is the integrated Planck function. Equating (A7) and (A8) leads to the following expression for temperature:

$$T^4 = \frac{\dot{A}}{4\kappa_P(T)\sigma}. \tag{A10}$$

Since $\kappa_P(T)$ is a function of temperature we solve this equation iteratively using pre-tabulated values of $\kappa_P(T)$.

Our code uses the Bjorkman & Wood (2001) technique for re-processing photon packets, and our modification of Lucy's (1999) path-length technique to determine the cell temperature. Since we assume that the opacity is not a function of temperature, we do not need to iterate to determine the temperature structure, as discussed in Bjorkman & Wood (2001).

A3 Dust destruction

Model discs used in this study extend from a sharply cut-off inner radius out to a specified distance. The inner radius is defined by the dust destruction temperature, which we take to be 1600 K. We make the simplifying assumption that the dust destruction radius is independent of latitude in the disc. The determination of the dust destruction radius is carried out after the temperature calculation and involves a nested loop that counts how many grid cells at each radius have temperatures below 1600 K. If this number is outside some specified range then the inner radius is shifted either towards or away from the central star. The disc density is then re-gridded, and the temperature calculation/dust destruction radius determination repeated. This continues until a stable radius is established. Once the inner radius is fixed the program starts to solve iteratively for density as described above.

A4 Iterative procedure

The program self-consistently solves for density using an iterative procedure. For the first iteration the analytic density structure of equation (1) is assumed, and this allows an initial temperature structure to be found. On the next iteration or at the point at which a suitable dust destruction radius has been established and a new grid set up, this temperature structure is used to determine a density structure using the numerical density technique. This density replaces the analytic density structure and the next iteration begins. The procedure continues until the temperature and density structure converges, typically within three iterations.

This paper has been typeset from a TEX/LATEX file prepared by the author.